Tuneable magnetic nanocomposites for remote self-healing.

GUPTA, R., GUPTA, P., FOOTER, C., STENNING, G.B.G., DARR, J.A. and PANCHOLI, K.

2022

scientific reports

Check for updates

OPEN

Tuneable magnetic nanocomposites for remote self-healing

Ranjeetkumar Gupta[1], Priya Gupta[2], Charles Footer[3], Gavin B. G. Stenning[4], Jawwad A. Darr[3]✉ & Ketan Pancholi[1]✉

When polymer composites containing magnetic nanoparticles (MNPs) are exposed to an alternating magnetic field, heat is generated to melt the surrounding polymer locally, partially filling voids across any cracks or deformities. Such materials are of interest for structural applications; however, structural polymers with high melting temperatures pose the challenge of generating high localised temperatures enabling self-healing. A method to prepare a multiferroic-Polyamide 6 (PA6) nanocomposite with tuneable magnetocaloric properties is reported. Tunability arises from varying the MNP material (and any coating, its dispersion, and agglomerate sizes in the nanocomposite). The superparamagnetic MNPs (SMNPs) and iron oxide MNPs with and without surface functionalization were dispersed into PA6 through in situ polymerization, and their magnetic properties were compared. Furthermore, computer simulations were used to quantify the dispersion state of MNPs and assess the influence of the interaction radius on the magnetic response of the self-healable magnetic nanoparticle polymer (SHMNP) composite. It was shown that maintaining the low interaction radius through the dispersion of the low coercivity MNPs could allow tuning of the bulk magnetocaloric properties of the resulting mesostructures. An in-situ polymerization method improved the dispersion and reduced the maximum interaction radius value from ca. 806 to 371 nm and increased the magnetic response for the silica-coated SMNP composite. This sample displayed ca. three orders of magnitude enhancement for magnetic saturation compared to the unfunctionalized Fe_3O_4 MNP composite.

Well-engineered magnetic nanocomposites with magnetocaloric capability are of interest in several engineering fields, including biomedical or structural self-healable magnetic nanoparticle polymer (SHMNP) composites[1–3]. Several groups worldwide are developing bulk polymer composites that can autonomously repair themselves through interaction with stimuli such as incident magnetic fields[4–6]. Furthermore, some of the authors recently reported the development of self-healing flexible composite pipelines using the magnetocaloric effect[7]. In that work[7], a composite multilayer tape consisting of a low melting temperature SHMNP sandwiched between a high melting point thermoplastic unidirectional fibre-reinforced prepreg or tape formed the basis of the self-healing pipe. When this tape was exposed to microwave radiation, the constituent polymer was shown to melt due to the magnetocaloric effect of nanoparticles dispersed within the structure[7]. This was due to the formation of a liquified (melted) polymer that filled the microcracks in the composite pipe (made up of unidirectional fibre-reinforced prepreg), causing the composite to self-heal. In this space, the optimization of the magnetic properties of the magnetic tape is essential for successful energy-efficient self-healing.

Many parameters, such as the choice of magnetic material, size and composition of MNPs, polymer type, and dispersion of MNPs in the polymer matrix, contribute to tuning the magnetocaloric properties of the SHMNP composites. Furthermore, maximisation of the saturation magnetisation to coercivity ratio for any material increases magnetocaloric efficiency. Low magnetic coercivity with appropriate degree of crystallinity is important to increase magnetic heating efficiency[8]. For example, the cubic phase crystalline gadolinium oxide nanoparticles with a low Curie temperature and coercivity is an ideal material with low coercivity for use in these self-healing structures, but its cost is prohibitive for the majority of applications[9].

[1]Advanced Materials Group, School of Engineering, Robert Gordon University, Aberdeen AB10 7GE, UK. [2]Lakshmi Narain College of Technology and Sciences, RGPV, Indore, MP, India. [3]Department of Chemistry, University College London, 20 Gordon Street, London WC1H OAJ, UK. [4]ISIS Neutron and Muon Facility, STFC Rutherford Appleton Laboratory, Didcot OX11 0QX, UK. ✉email: j.a.darr@ucl.ac.uk; k.pancholi2@rgu.ac.uk

SHMNP composites sample in text	SHMNP composites sample description	SCN (w/w %)	NPC (w/w %)
Sample A	PP	–	–
Sample B	Un-Fe_3O_4	0	1.0
Sample C	TEOS-Fe_3O_4	2.4	1.0
Sample D	Un-SMNP	0	1.0
Sample E	TEOS-SMNP	2.4	1.0

Table 1. Details of the prepared samples. *PP* pristine polymer (PA6), *Un-Fe_3O_4* uncoated Fe_3O_4, *TEOS-Fe_3O_4* silica coated Fe_3O_4, *Un-SMNP* uncoated superparamagnetic MNP, *TEOS-SMNP* silica coated superparamagnetic MNP, *SCN* silica coating on MNPs, *NPC* MNP concentration in SHMNP composites.

In SHMNP composites, the high overall interfacial area offered by adding a small amount of MNPs with a high surface area-to-volume ratio enhances magnetic properties[10,11]. Though controlling the dispersion of the MNPs in the polymer matrix, it is essential to achieve desirable magnetocaloric properties. The interaction of local magnetic fields of neighbouring large agglomerates of MNPs has been shown to decrease the magnetocaloric effect in some polymer composites[3]. To reduce the agglomeration size of MNPs and increase dispersion, surface functionalization (coating) of particles can be used in SHMNP composites.

Herein, the authors present a specific method of preparing several SHMNP composites from surface-functionalised (coated) MNPs and polyamide 6 (PA6). To evaluate the effect of dispersion and magnetic material composition of MNPs on the magnetisation and thermomagnetic properties of the prepared SHMNP composite samples, four types of samples were prepared—two with 1 w/w% Fe_3O_4 MNPs and two with 1 w/w% superparamagnetic MNPs (SMNPs). Further details of the sample contents and their nomenclature can be found in Table 1. The resulting magnetic properties showed some dependency on the silica functionalization (coating) of MNPs and on the preparation technique of the SHMNP composites. Superparamagnetic MNPs[12] (synthesized by University College London authors) may be considered promising candidates for achieving a low Curie temperature at lower cost than other potential MNP filler options. The improvements in the dispersion state of MNPs and their interparticle interactions were assessed, as well as their resulting magnetic multifunctionality.

Results and discussions

Establishing the correlation between particle dispersion state, magnetic particle properties including crystallinity and polymer crystallinity is required for optimizing the properties of the manufactured SHMNP composites. Thus, the dispersion states for four different SHMNP composite samples (Table 1) were evaluated using transmission electron microscopy (TEM), X-ray diffraction (XRD) and small and wide-angle X-ray scattering (SAXS/WAXS) and compared with the pristine synthesized PA6 polymer. The average MNP size and agglomerate size distribution within the SHMNP composites were estimated from SAXS/WAXS data through implementation of the Guinier and Porod law[3]. The calculated average MNP/agglomerate size was then used to build a 3D model for visualization. Furthermore, the magnetic properties of the MNPs and their SHMNP composites at temperatures of 100 and 400 K, respectively, were measured using a superconducting quantum interference device (SQUID) detection system (Quantum Design MPMS 3 integrated SQUID). To estimate the magnetocaloric properties, field-cooled (FC) and zero-field-cooled (ZFC) magnetization curves for the SHMNPs were obtained at various magnetic field strengths. This information was then correlated with the dispersion state. All characterization methods are described in detail in Supplementary Data Section S1.

The magnetic properties of the SHMNP composites include the ability to respond to even a small magnetic field and be capable of generating a sufficiently high temperature to melt a structural polymer similar to PA6. The presence of MNPs in the SHMNP composite reduces the overall melting temperature (due to a drop in the degree of crystallinity due to MNPs); however, a small crystallite size was ensured via the SHMNP composite processing methodology.

Chemical composition of the prepared PA6 SHMNP composite samples. Attenuated total reflectance-Fourier transform infrared (ATR-FTIR) spectral data for pure PA6 and all SHMNP (Fig. 1) composites were used to confirm the successful synthesis of PA6 by matching peaks associated with commercial grade PA6 reported in the literature[13]. As seen in Fig. 1, peaks related to methylene (CH_2) asymmetric and symmetric stretching vibrations for the absorbance bands related to PA6 were observed in the ranges 2931 to 2938 cm^{-1} and 2860 to 2866 cm^{-1}, confirming the formation of PA6[13,14]. Prominent absorbance bands corresponding to N–H stretching and hydrogen bonding were observed for the as-made and commercial samples in the range[3] 3294 to 3298 cm^{-1}. In addition, this absorbance band also confirmed the presence of the amide II band (of primary amides), which occurred due to stretching vibration of the C=O double bond, which can be further attributed to the functionality of the amide I band. Additional peaks were also seen ca. 1540 cm^{-1}, relating to the previously mentioned primary type amide I and II bands but also the vibrations due to stretching of the C-N bond, which was accompanied by peaks due to bending of the N–H bond and the CO–NH bend[15].

As seen in Fig. 1, the level of crystallinity of the SHMNP composite increased with MNP silica surface functionalization, which was confirmed by the observation of a shift in the N–H bending peaks from 1531 to 1537 cm^{-1} in samples C and E[14]. The degree of crystallinity was generally dictated by the position and intensity of these crystalline bands, as well as the broader bands from the amorphous phase[16]. It was inferred that the degree

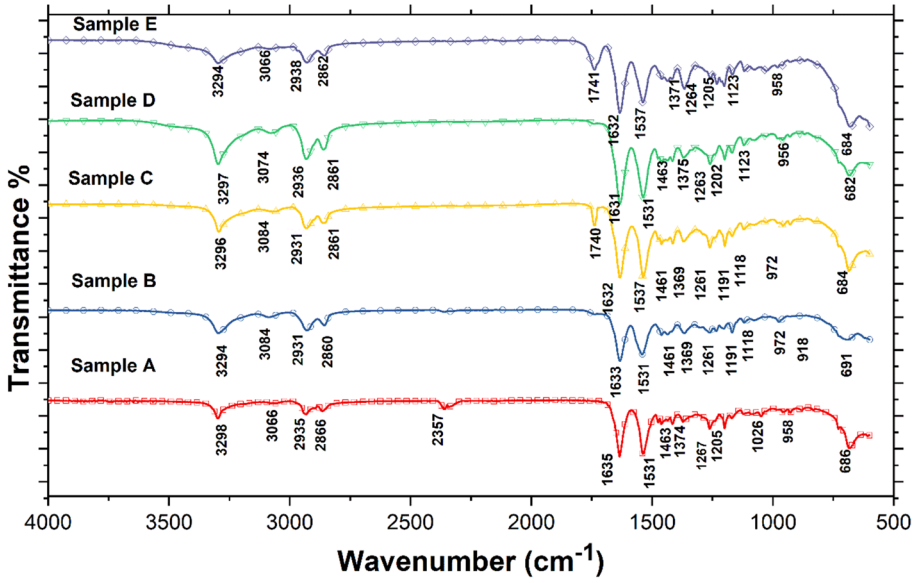

Figure 1. ATR-FTIR spectra of polymer and SHNMP composite samples.

of crystallinity was moderately high in the SHMNP composite samples with the uncoated MNPs, as the amide II band (sensitive to crystallinity) appeared at approximately 1531 cm^{-1} in the spectra of samples B and D. The wavelength fingerprint for carboxylic acid (C=O stretch), a product from the hydrolysis of tetraethyl orthosilicate (TEOS) during the MNP coating process, is typically ca. 1700 cm^{-1}, however, the closest corresponding absorbance band observed, was a small broad peak near the peak[17] at ca. 1740 cm^{-1}.

Effect of silica coating on dispersion of nanoparticles. A good dispersion state of MNPs within SHMNP composites ensures a high polymer crystallinity, small crystallite size and uniform magnetic saturation, which is essential for efficient self-healing and mechanically strong joints. In the preparation of SHMNP composites, the MNPs were functionalized (coated with silica before being added to the PA6 matrix) to improve their dispersion state. To quantify the improved MNP dispersion state due to silica coating, the TEM images of SHMNP composites were analysed. The TEM images of the microtome SHMNP composite slices showed that the dispersion of MNPs (or their agglomerates) was improved with MNP silica coatings (see Fig. 2iii,iv). As seen in Fig. 2i,ii, the uncoated MNPs in samples B and D formed larger agglomerates due to high dipole–dipole interparticle attractions.

The TEM images only provided information on the dispersion state of the MNPs in an area of a few square micrometers. Therefore, SAXS/WAXS data were employed to help evaluate the dispersion state on a broader scale (microvolume) than TEM images. To determine the extent of dispersion, the SHMNP composites were characterized using SAXS/WAXS techniques. The filler structure and structure of polymer chains inside MNP-polymer composites (similar to SHMNP composites) have been previously studied with scattering techniques, including XRD and SAXS/WAXS[18]. Statistical mechanical theories relate the dispersion state (which dictates the space configuration of the nanoinclusions) to stress within the polymer[19], and this nanoscale stress correlates to the size of inclusions/agglomerates. This helped elucidate MNP sizes within the SHMNP composite, including for complex agglomerates of MNPs[20].

Figure 2v represents the scattering intensity I(q), plotted as a function of the scattering vector q for all the samples studied. The SAXS profile of the Guinier-type plot (Supplementary Data Section S2) was comprised of a flat region due to the polymer response (as is very clear from the pristine PA6 data plot) and a region with a steep gradient related to the response from the MNPs in the samples. The cumulatively slope-dropping region is a characteristic of the Porod scattering response from MNPs[21]. The Guinier region precedes the Porod region, wherein the scattering of the former reflects the radius of gyration of the scatterers as per Guinier's law[21]. By calculating the radius of gyration (R_g), the average diameter (D) of MNPs in a volume of SHMNP composites was estimated. These data are summarised in Table S1, while a detailed analysis of the SAXS data is discussed in Supplementary Data Section S2.

The average diameter (D) of MNPs calculated from the SAXS data was found to be in broad agreement with the values obtained from TEM image analysis. Samples C and E have the lowest average diameter of MNP/agglomerates.

Effect of MNP dispersion on the crystallinity of SHMNP composite samples. The differential scanning calorimetry (DSC) results for all the samples, as seen in Fig. 3a, exhibited noticeable endothermic peaks (melting) and clearly depicted the glass transition temperature of all polymer-based samples. The results of the thermal analysis represent the glass transition temperature (T_g) occurrence of the pristine polymer at ca. 46 °C, which was similar to previously reported values[22]. The melting temperature (T_m) observed in the DSC

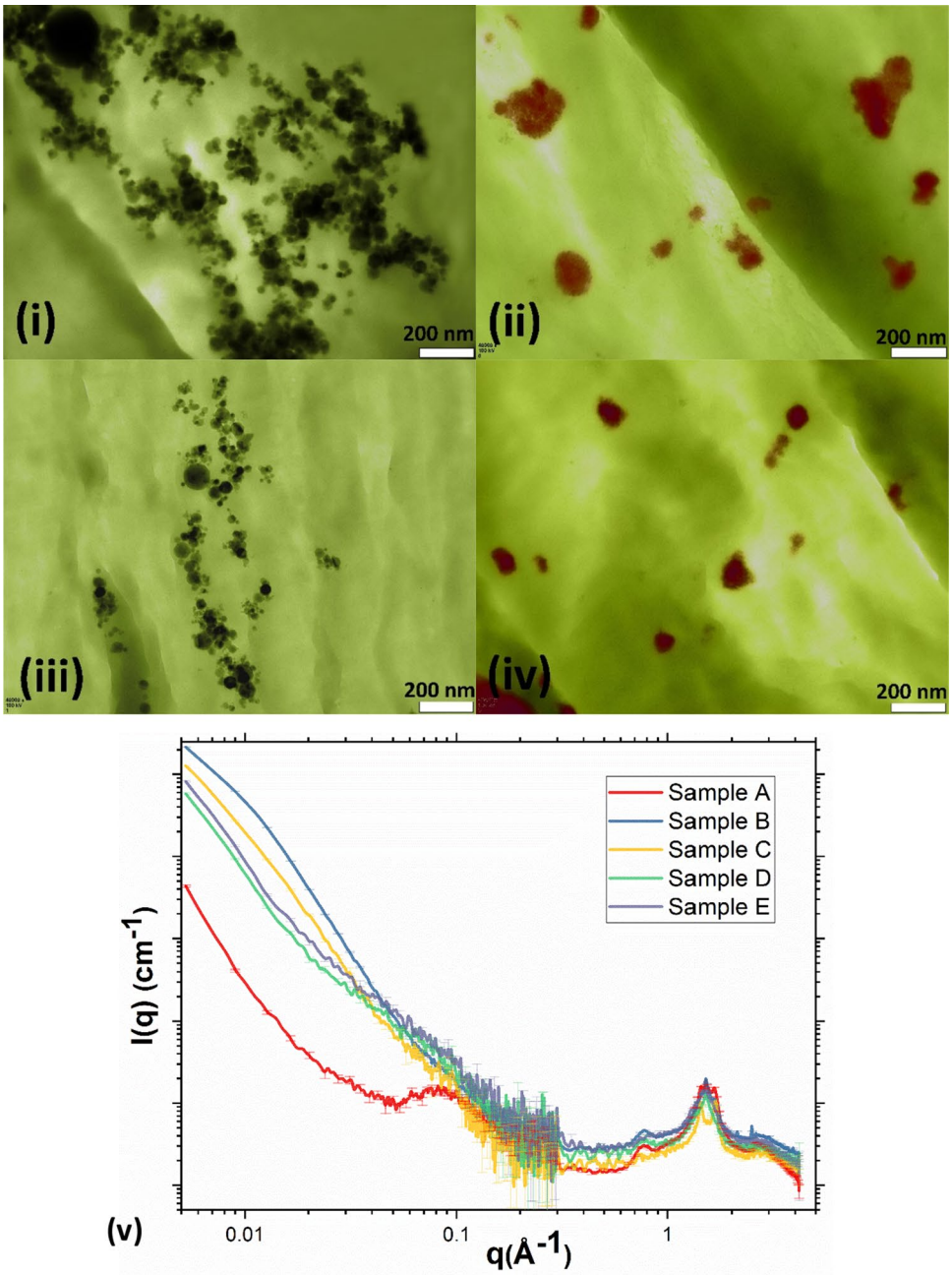

Figure 2. Postprocessed TEM images for microtome sections of nanocomposites containing uncoated samples (**i**) sample B and (**ii**) sample D and nanocomposites containing coated samples, (**iii**) sample C and (**iv**) sample E. (The scale bar shown is 200 nm.) The Fe_3O_4 and superparamagnetic MNPs are observed as black and red colours, respectively. (**v**) Background corrected SAXS (0.005–0.3 $Å^{-1}$) and WAXS (0.3–4.17 $Å^{-1}$) intensities I(q) as a function of the scattering vector 'q' for all the samples studied.

results was slightly lower than the published values ca. 220 °C[22]. Additionally, as seen from Table S2 (included in Supplementary Data Section S3), the melting temperature of the SHMNP composite was found to slightly increase for the samples containing silica-coated MNPs. However, the T_g values were shown to increase due to the MNP silica coating; the increased wetting of the surface-modified MNPs by the polymer is known to decrease the crystallinity of the nanocomposite and hence increase T_g but decrease the melting temperature[23].

The DSC results also confirmed that wetting of the MNPs by the polymer melt was increased as a result of no particle coating on the MNPs. With no coating on the surface of MNPs, this promoted strong attractive interactions with other particles and in turn with surrounding polymer chains, leading to reductions in cooperative segmental mobility in the polymer and an increase in T_g[23–25]. The melting endotherm values as presented in the DSC plot in Fig. 3a represent the amount of heat stimuli required to bring about the melt response for each sample. Stating that the samples B to E in real application for structural healing would require minimum heat stimuli of

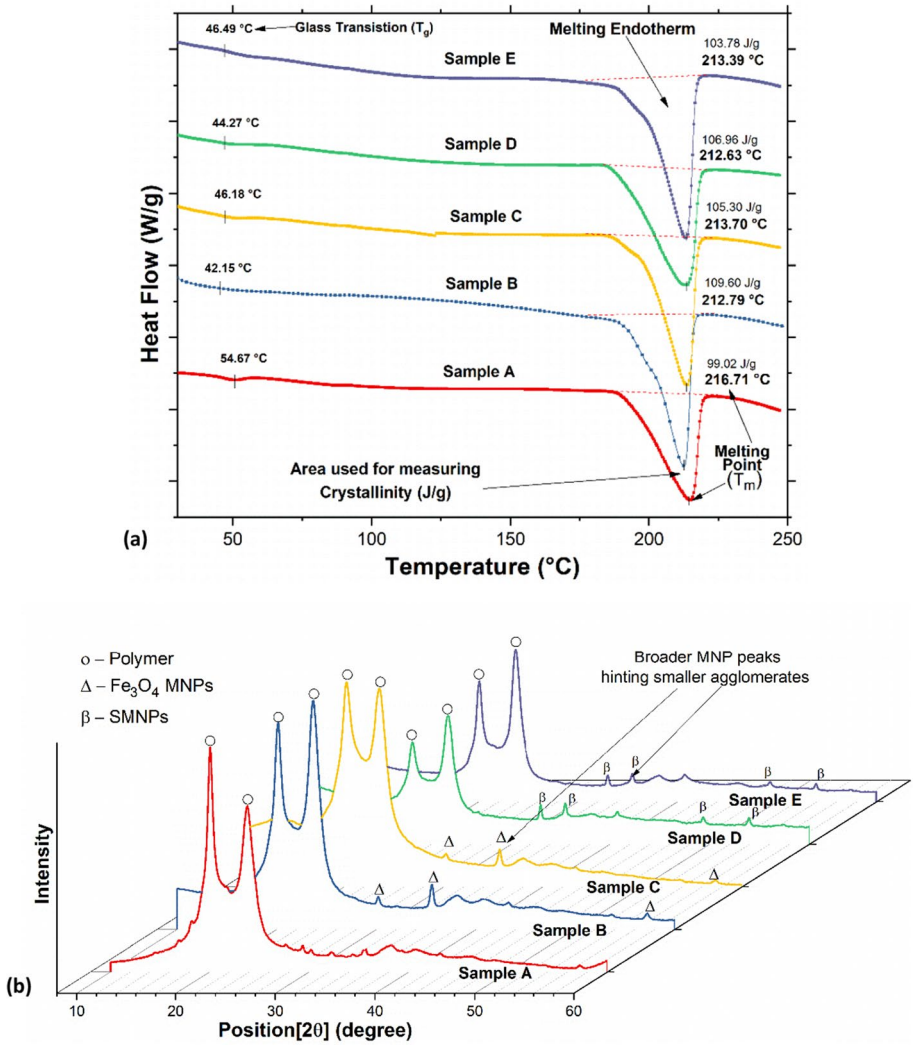

Figure 3. (**a**) DSC curves of all the prepared SHMNP composite samples A to E, showing the glass transition temperatures and melting points and (**b**) XRD patterns of all the prepared SHMNP composite samples A to E.

at least 109.60 J/g, 105.30 J/g, 106.96 J/g and 103.78 J/g respectively. Further, information about the crystallinity of nanocomposites was suggested from the XRD results. As seen in Fig. 3b, the main characteristic XRD peaks for the nanocomposite gave a good match to those in the reference pattern JCPDS file number 82-1533; peaks were observed for (hkl) values of (220), (311), (400), (511) and (440) at 2 theta values of 30.3°, 35.4°, 43.1°, 57.3° and 62.7°, respectively. The crystallite sizes of MNPs were estimated from the FWHM of the most intense XRD peaks using the Debye–Scherer formula (as listed in Table S3 in Supplementary Data Section S4).

The two broad crystalline peaks in the XRD data associated with SHMNP materials containing samples C and E showed an increase in crystallinity (sharper peaks) compared to the pristine polymer sample (sample A) and SHMNP samples incorporating uncoated MNPs (samples B and D). This confirmed that the degree of crystallinity changed due to MNPS surface functionalization. Additionally, as observed in Fig. 3b, the silica functionalization of MNPs somewhat suppressed the intense MNP phase-related XRD peaks in samples C and E. In contrast, composites containing samples B and D showed significant broadening and minimal intensity in the comparative XRD data. Once a coating was applied to the MNP, a nonmagnetic silica layer formed on the surface that appears to reduce particle–particle interactions, and hence, the mean crystallite size or agglomerate size was reduced (see Table S3 in Supplementary Data Section S4).

Magnetic and thermomagnetic response of MNPs and SHMNP composites. It should be noted that the particle aggregation effects were particularly apparent only in the case of low MNP contents; hence, the authors only tested the SHMNP composites with 1 wt% MNPs. The effect on the magnetic response suppression due to the silica coating was evaluated and is discussed here. The magnetic properties of the MNPs with and without functionalization and all the synthesized SHMNP composite samples were assessed by magnetization curves at temperatures of 100 and 400 K. The hysteresis loops showed ferromagnetic behaviour, although the variation due to the dispersion of MNPs resulting from silica coating was clearly distinguishable, as seen in

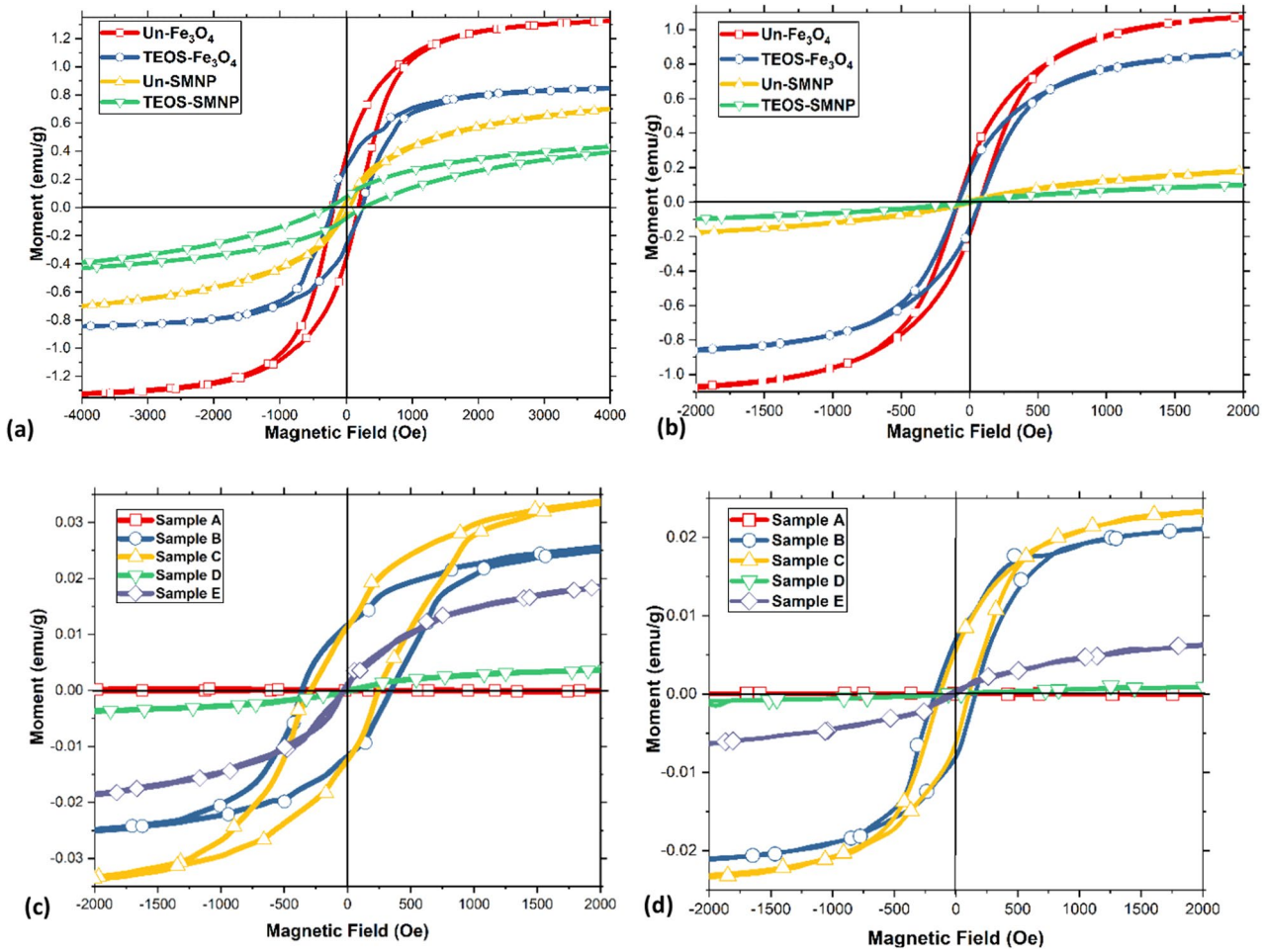

Figure 4. Magnetization hysteresis (M-H) loops for (**a**) MNP samples at 100 K, (**b**) MNP samples at 400 K, (**c**) SHMNP composite samples at 100 K and (**d**) SHMNP composite samples at 400 K.

Fig. 4a,b. On application of a homogeneous magnetic field of 50,000 Oe (full-scale plots included in Supplementary Data Section S5) at 100 K, the MNPs showed a magnetic moment ratio (M_r/M_s) of remanence magnetization (M_r) to saturation (M_s), as listed in Table S4 (in Supplementary Data Section S5), of 28.0 and 6.8% for uncoated Fe_3O_4 and superparamagnetic MNPs, respectively; for coated Fe_3O_4 and SMNPs, it was 34.2 and 7.7%, respectively, at 400 K (as listed in Table S5 in Supplementary Data Section S5), and the ratio was 17.1 and 1.4% for uncoated MNPs and 15.1 and 0.9% for coated MNPs, respectively. Here, the drop in the magnetic moment ratio was observed with the silica coatings of MNPs as a result of suppression of the magnetic remanence caused by the diamagnetic silica layer on the surface.

Furthermore, the SHMNP composite measurements at 100 K (Fig. 4c and Table S6 in Supplementary Data Section S5) showed a magnetic moment ratio of 0% for sample A and 40.9, 31.1, 3.0 and 1.5% for MNP samples B, C, D and E, respectively. The measurements at 400 K (Fig. 4d and Table S7 in Supplementary Data Section S5) revealed magnetic moment ratios of 33.5, 25.1, 19.6 and 2.8% for MNP samples B, C, D and E, respectively.

After increasing the temperature to 400 K, the M_r/M_s ratio decreased significantly for all samples compared to small reduction observed for sample D (Fig. 4c,d), suggesting an uneven dispersion or agglomeration of MNPs. The high degree of agglomeration in sample D was further confirmed by the XRD data and small-angle scattering results. The observation of the wide hysteresis loop at the lower temperature of 100 K (compared to that at the higher temperature of 400 K) hinted towards the superparamagnetic behaviour induced in the designed SHMNP composites[19]. The SMNP samples (D and E) showed almost zero coercivity and a significant superparamagnetic response[26] compared to samples B and C, which contained Fe_3O_4 nanoparticles. The hysteresis loops of the Fe_3O_4 SHMNP composites revealed symmetric behaviour similar to that of ferromagnetic materials[27], confirming the suitability of the synthesized SHMNP composites for magnetic stimuli-based self-healing applications in structural composites. The magnetic remanence in the silica-coated SMNP-containing sample E was almost zero (ca. 2–3%) compared to the sample containing the coated Fe_3O_4 (sample C). This suggested that the former SHMNP composites (sample E) had a short Neel relaxation time in response to the applied magnetic field. The coercivity of all Fe_3O_4 SHMNP composite samples (samples B and C) had values in the ranges of 270–310 Oe and 110–120 Oe (except the pristine sample, which showed zero magnetization) at temperatures of 100 and 400 K,

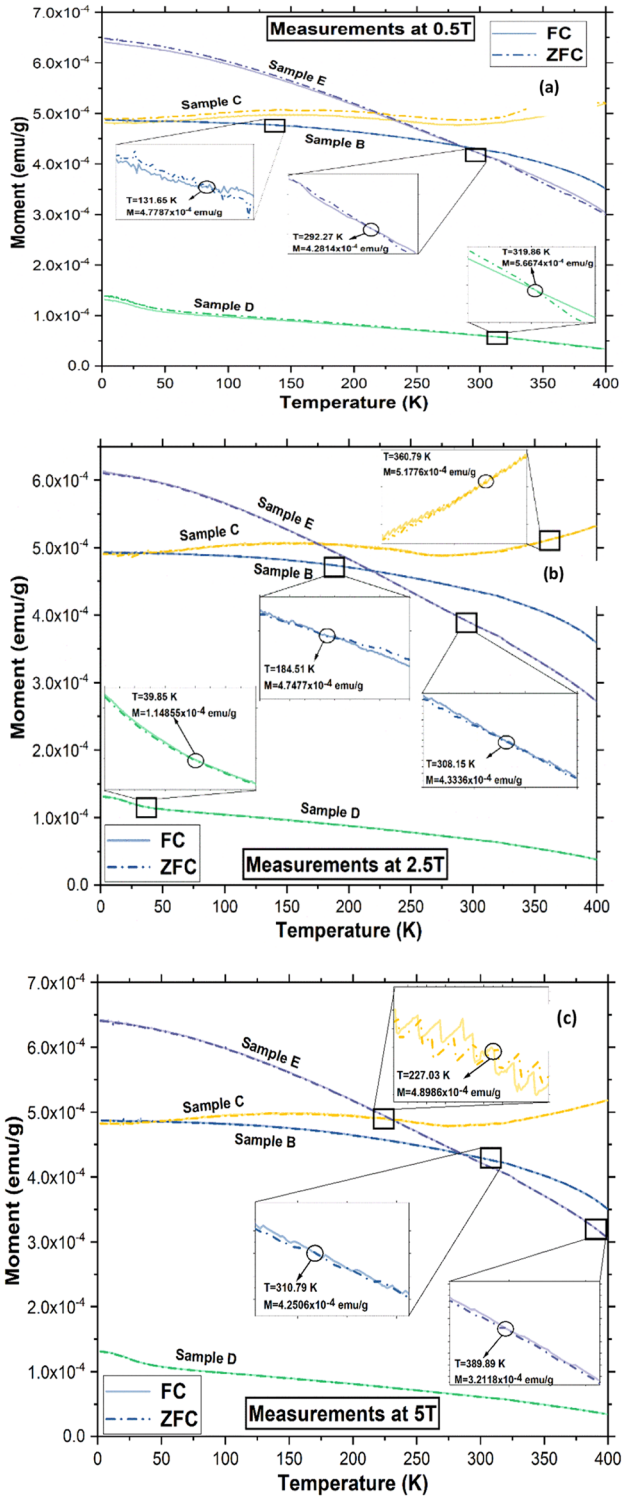

Figure 5. Field cooled (FC) and zero field cooled (ZFC) response for SHMNP composite samples B, C, D and E at (**a**) 0.5 T, (**b**) 2.5 T, and (**c**) 5 T.

respectively. However, the coercivity for all SHMNP composite samples (samples D and E) was low because of the decrease in the strength of the dipole–dipole interaction.

The FC/ZFC (field cooling/zero field cooling) curves for all the SHMNP composite samples at 0.5, 2.5 and 5 T magnetic fields are shown in Fig. 5. Variation in the magnetic field showed a small divergence between the ZFC and FC curves (zoomed in inset figure), which occurred in the temperature range of 132 to 320 K. As the field strength was increased, the ZFC–FC crossing temperature increased for SHMNP composite samples B, C

and E; however, the trend was absent in SHMNP composite sample D due to high agglomeration. The Curie temperature can be determined from d^2M/dT^2 calculations. These values are included in Fig. 5; however, small peaks other than Curie temperature peaks were also observed, which can be attributed to the polymer matrix surrounding the MNPs. Typically, FC/ZFC curves provide information about effective anisotropy (K_{eff}), which encompasses crystal, shape, and surface anisotropy in a single parameter. However, there was a remarkable absence of the Verwey transition, a metal-to-insulation transition of MNPs at a certain temperature range, often associated with a downward or upward change in the coercive field (Hc) values[28], which was found to be absent for SHMNP composite samples D and E. This implied that the reduction or complete loss of the Verwey transition for SMNPs was possible if they were added into a polymer matrix. For instance, some recent reports indicate a strong reduction[26] or even a complete loss[27] of the Verwey transition temperature in SHMNP composites. Furthermore, there were signs of disappearance of hysteresis in Fig. 4c,d for SHMNP composite samples B and C and SHMNP composite sample D, indicating that they had almost become magnetically unblocked, almost reaching a thermal equilibrium state at lower temperatures. In contrast, SHMNP composite sample E showed a distinct behaviour compared to the other SHMNP composite samples (its FC and ZFC curves gradually approached each other), and the observed blocking temperature was higher at temperatures near 400 K, where both curves crossed each other. The increase in field strength was directly proportional to the blocking temperature for SHMNP composite samples B and E; however, this was not true for other SHMNP composite samples B and E, likely due to the inhomogeneous dispersion of MNPs in the weakly paramagnetic polymer matrix. The trend shows that the blocking temperature increased at a higher field strength, which was helpful in melting the polymer surrounding the dispersed MNPs without their transition to the paramagnetic phase, therefore stopping heat production. This is useful for self-healing SHMNP composite applications where localized polymer melting is the primary aim[3]. These data can be used for calculating the particle distribution based on the magnetic response of the SHMNP composite sample and were added to support the SHMNP composite model using simulated data. To understand the effect of material type and dispersion state on the magnetocaloric properties of the SHMNP composite, an interaction radius model was constructed.

Interrelation of the dispersion state of MNPs with the magnetic response. The equivalent diameter of the ellipsoidal nanoparticles within the SHMNP composites was estimated using ImageJ software and following the method explained elsewhere[29,30]. The estimated average diameter (Table S8 in Supplementary Data Section S6) for each sample was then used as input data in MATLAB® code to simulate the 3D model.

To simplify the simulated model, all the entities were generated as only spherical nanoparticles/agglomerates. The simulated models for all the SHMNP composite samples are included in Supplementary Data Section S6, where each sphere represents the small- to large-size agglomerates of MNPs. The purpose of this modeling was to visualize and interpret the dispersion state of the synthesized SHMNP composite samples with and without the MNP surface functionalization effect, which was quite challenging to obtain with physical characterization methods alone. The magnetic interaction (either dipolar or exchange) between neighbouring MNP agglomerates in each SHMNP composite sample was estimated by calculating the interaction radius (IR) for each nanoparticle/agglomerate generated as individual spheres of variable sizes in the model, as seen in Fig. 6a–d. The IR values, summarised in Table 2, considered the nearest neighbor condition, i.e., the distance between the nearest neighbouring agglomerates in the model. These data were used to graphically represent the interaction region, as shown in Fig. 6a–d, and subsequently, they were correlated with the magnetic behavior of all SHMNP composite samples in Fig. 6e.

Interestingly, the simulated models demonstrate that the IR was a variable term dependent on the size of the agglomerates and on the nearest possible neighbours. From Table 2, it can be observed that the minimum and maximum IR values for all SHMNP composite samples were reduced by ca. 50 and 430 nm, respectively, as a result of MNP coating.

Interrelating the IR data of all the samples with that of the observations from TEM micrographs, SAXS/WAXS and XRD data, the results combined suggest that functionalization (silica coating) of the MNPs was more effective in reducing agglomeration within the polymer matrix in the case of Fe_3O_4 than that of the SMNPs. The possible reason for this can also be that the dipole–dipole type interparticle attraction among the silica-coated SMNPs was higher than that among the coated Fe_3O_4 MNPs.

A high blocking temperature is required for applications such as structural self-healing, where the surrounding polymer matrix should melt to heal cracks and deformities in the material structure. If heating of the MNPs stops at lower temperatures, the materials will not melt high modulus polymers such as PA6. The requirement of achieving high temperature overrides the efficiency goal. To assess the key parameters required to achieve the requirement, the data on the interaction ratio (IR) and blocking temperature values were used.

As seen in Fig. 6e, the value of blocking temperature derived from the ZFC–FC magnetisation data is plotted against the IR for various applied magnetic fields. Low values of IR seemed to be related to higher blocking temperatures. Even with the higher IR value of 173, the blocking temperature for SHMNP composite Sample E was found to be mostly higher than the temperature for SHMNP composite sample C with IR -139 at all applied magnetic field strengths except 2.5 T. The IR value difference between SHMNP composite samples C and E was small enough; however, SHMNP composite sample D (containing uncoated SMNP) with a high IR value of 394 showed a low blocking temperature compared to SHMNP composite sample B (containing uncoated Fe_3O_4 MNPs) under an applied field strength of 2.5 T. This could be attributed to an inhomogeneous external magnetic field. From these observations, it can be deduced that the low coercivity and superparamagnetic behaviour of SMNPs in SHMNP composite samples E and D contributed to higher blocking temperatures. When considering the magnetic properties of the MNPs (superparamagnetic, low coercivity), the IR value was a good parameter to determine the efficiency of magnetocaloric properties. Looking at the IR values in Table 2, it seems that particle

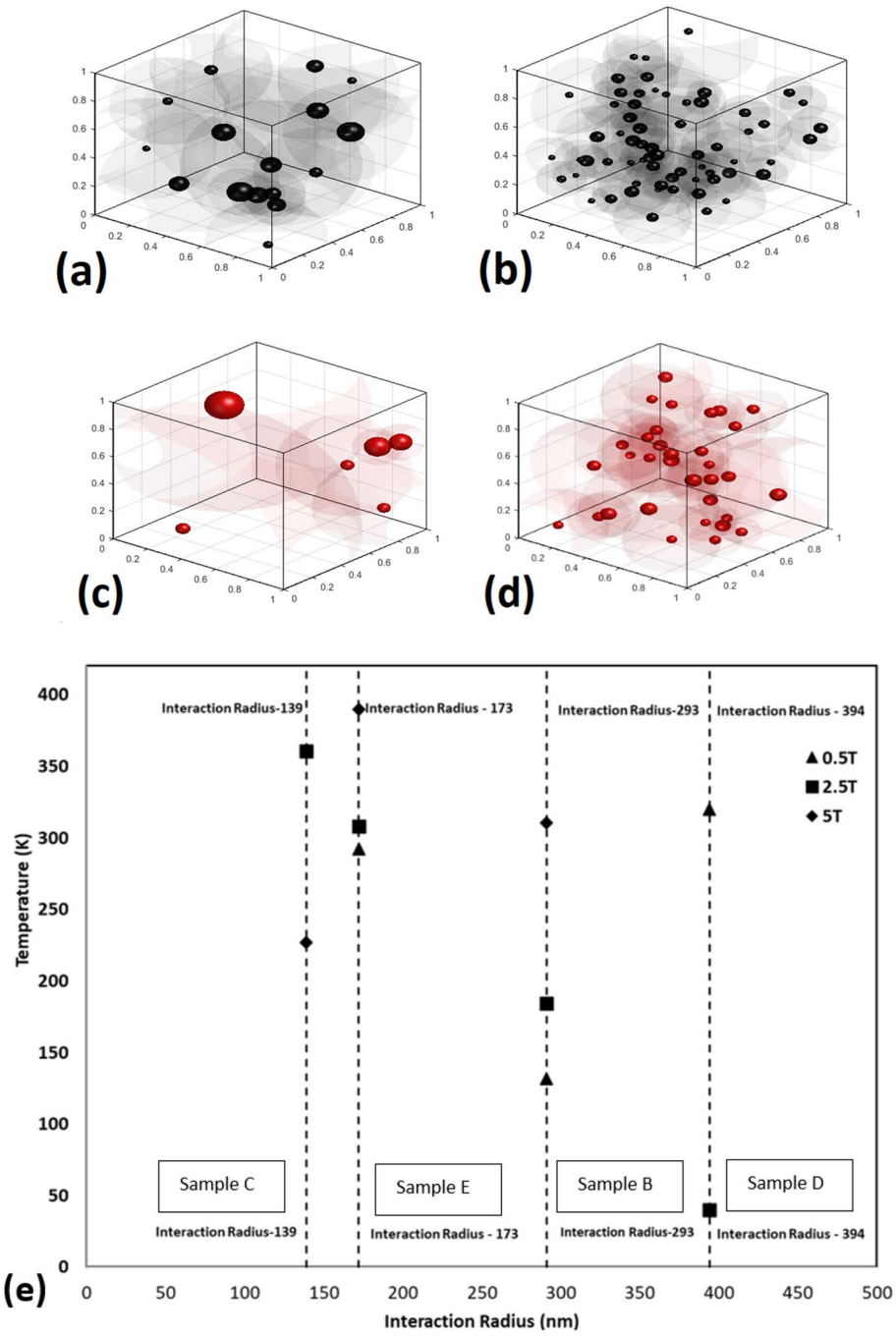

Figure 6. Simulated representation included with the interaction radius (IR) of the individual nanoparticle/agglomerates present in the synthesized nanocomposite (1 μm^3) for Fe_3O_4 samples (**a**) sample B, (**b**) sample C and superparamagnetic samples (**c**) sample D, (**d**) sample E, respectively (herein, black spheres represent Fe_3O_4 and red spheres are for superparamagnetic nanoparticle/agglomerates, respectively.) (**e**) Correlation between blocking temperature and interaction radius of the SHMNP samples.

dispersion also played an important role, along with the intrinsic properties of the filler material. The blocking temperature values seem to be related to the coercivity values rather than the saturation magnetization. SHMNP composite sample E displayed low IR values and showed a roughly linear increasing trend compared to SHMNP composite samples D and B (with uncoated MNPs), which was associated with the greater particle agglomeration in SHMNP composite samples D and B. Moreover, magnetocaloric effects are known to be related to coercivity values rather than the magnetic saturation value for most materials[31]. These low coercivity MNPs and their dispersion state[32] in the synthesized SHMNP composites determined the resulting magnetocaloric behaviour. However, it was not applicable to MNPs with a size greater than 100 nm[33]. For nanocomposites, an efficient design requires good dispersion and low coercivity materials.

Sample	Minimum interaction radius (nm)	Maximum interaction radius (nm)	Average interaction radius (nm)	Standard deviation (nm)
Sample B	123	448	291	109
Sample C	77	345	139	55
Sample D	117	806	394	262
Sample E	65	371	172	78

Table 2. Summary of the calculated interaction radius values for each sample.

The amount of heat generated is correlated to the change in the magnetic entropy in the system[34]. To estimate the heat generation, the change in entropy ΔSm was approximated using the isotherm M-H curves[35] at 100 K and 400 K. Using the limited data, the calculated values of ΔSm were found to be highest for SHMNP and SHMNP composite with magnitude in region of 20.5 J K^{-1} kg^{-1} and 0.1 J K^{-1} kg^{-1}, respectively. The values for change in entropy demonstrates that SHMNP and SHMNP composite, both will generate highest heat in response to alternating magnetic field.

Correlation between magnetic properties and thermomagnetic properties. As seen in the Fig. 5a–c, the magnetic moment for sample E (superparamagnetic materials) was found to be highest at 2.5 T amongst all samples. Moreover, the low coercivity and small area enclosed by the M-H hysteresis curve shows low losses for the sample E, which has a highest magnetisation 6.5×10^{-4} emu/g at lowest temperature. The trend showed that the lower the coercivity or remanence of nanoparticles, higher the magnetisation in relation to temperature. The excellent magnetocaloric effect depends on the heat capacity Cp (T) and isothermal change in the magnetic contribution into the entropy ΔSm[36]. The ΔSm is proportional to the difference between the measured magnetisation values at lowest and highest temperature. From the Fig. 5, it can be concluded that the low coercivity of the nanoparticle materials is responsible for generating the higher ΔSm in the material and thus, the higher temperature generation in response to exposure of the alternative magnetic field[36].

Conclusions

Using a viable method, the correlation between the magnetic properties of SHMNP composites, the dispersion state and filler material of MNPs, was established, and a clear understanding of the interaction between the dispersion state and the material properties in the SHMNP composites was developed. 3D modeling of the MNP dispersion and magnetic properties of the SHMNP composites showed that a lower calculated interaction ratio equated to a better dispersion. The TEM, XRD and SAXS characterization results showed that silica functionalization on the MNPs reduced the interaction ratio and, therefore, improved the dispersion of the filler materials. To prepare self-healable PA6 nanocomposites suitable for structural applications, it is essential to coat the MNPs such that they provide good dispersion but retain their magnetic properties. Moreover, to achieve high temperature in composites for local melting of the polymer phase (for self-healing of the structure), low coercivity MNPs should be used. The SHMNP composite prepared using the silica-coated SMNPs (containing particles with superparamagnetic behaviour) showed exceptional magnetic behaviour compared to any other magnetite-containing SHMNP composite samples reported, with almost zero coercivity and the least remanence magnetization (including enhanced superparamagnetic response) compared to the paramagnetic Fe_3O_4 SHMNP composites. Such a material with a low interaction radius is presumed to be the most suitable for self-healable polymer nanocomposites suitable for structural applications.

Data availability

All data needed to evaluate the conclusions in the paper are presented in the paper and/or the Supplementary Materials. The datasets generated and/or analysed during the current study are available in the public OpenAir repository, https://rgu-repository.worktribe.com/output/1579700.

Received: 20 January 2022; Accepted: 11 May 2022
Published online: 17 June 2022

References

1. Kalia, S. *et al.* Magnetic polymer nanocomposites for environmental and biomedical applications. *Colloid Polym. Sci.* **292**, 2025–2052 (2014).
2. Thévenot, J., Oliveira, H., Sandre, O. & Lecommandoux, S. Magnetic responsive polymer composite materials. *Chem. Soc. Rev.* **42**, 7099–7116 (2013).
3. Gupta, R. *et al.* Novel method of healing the fibre reinforced thermoplastic composite: A potential model for offshore applications. *Compos. Commun.* **16**, 67–78 (2019).
4. Scheiner, M., Dickens, T. J. & Okoli, O. Progress towards self-healing polymers for composite structural applications. *Polymer* **83**, 260–282 (2016).
5. Du, G. *et al.* Nacre-mimetic composite with intrinsic self-healing and shape-programming capability. *Nat. Commun.* **10**, 1–8 (2019).
6. Kessler, M., Sottos, N. & White, S. Self-healing structural composite materials. *Compos. A Appl. Sci. Manuf.* **34**, 743–753 (2003).
7. Gupta, R. *et al. Integrated Self-Healing of the Composite Offshore Structures* (OCEANS 2017-Aberdeen, IEEE, 2017).
8. Martins, P. & Lanceros-Mendez, S. *Advanced Lightweight Multifunctional Materials* 391–405 (Elsevier, 2021).

9. Cheng, Y. *et al.* Polymer-based gadolinium oxide nanocomposites for FL/MR/PA imaging guided and photothermal/photodynamic combined anti-tumor therapy. *J. Control. Release* **277**, 77–88 (2018).
10. Gupta, R. *et al.* Effect of oleic acid functionalised iron oxide nanoparticles on properties of magnetic polyamide-6 nanocomposite. *J. Miner. Metals Mater. Soc. (TMS)* **71**, 3119–3128 (2019).
11. Srinivasan, S. Y. *et al.* Magneto-conducting core/shell nanoparticles for biomedical applications. *ChemNanoMat* **4**(2), 151–164 (2018).
12. Darr, J. A., Zhang, J., Makwana, N. M. & Weng, X. Continuous hydrothermal synthesis of inorganic nanoparticles: Applications and future directions. *Chem. Rev.* **117**, 11125–11238 (2017).
13. Xu, G., Lu, W., Feng, X. & Yu, S. Self-assembly of organic–inorganic nanocomposites with nacre-like hierarchical structures. *Soft Matter* **7**, 4828–4832 (2011).
14. Choi, E.-Y. *et al.* Reinforcement of nylon 6,6/nylon 6,6 grafted nanodiamond composites by in situ reactive extrusion. *Sci. Rep.* **6**, 37010. https://doi.org/10.1038/srep37010 (2016).
15. Pockett, J. Crystallinity in linear polyamides: a study using melt blending with small-molecule diluents (2004).
16. Yang, F. *et al.* Influence of pH on the fluorescence properties of graphene quantum dots using ozonation pre-oxide hydrothermal synthesis. *J. Mater. Chem.* **22**, 25471–25479 (2012).
17. Larkin, P. IR and Raman Spectra—Structure Correlations: Characteristic Group Frequencies. Infrared and Raman Spectroscopy, 73–115 (2011).
18. Thomas, S., Rouxel, D. & Ponnamma, D. *Spectroscopy of Polymer Nanocomposites* (William Andrew, 2016).
19. Doi, M. & Edwards, S. F. *The Theory of Polymer Dynamics* 140–176 (Oxford University Press, 1988).
20. Teixeira, J. Small-angle scattering by fractal systems. *J. Appl. Crystallogr.* **21**, 781–785 (1988).
21. Porod, G., Glatter, O. & Kratky, O. *Small Angle X-ray Scattering* 17 (Academic Press, 1982).
22. http://www.polymerprocessing.com/polymers/PA6.html
23. Rittigstein, P. & Torkelson, J. M. Polymer–nanoparticle interfacial interactions in polymer nanocomposites: Confinement effects on glass transition temperature and suppression of physical aging. *J. Polym. Sci. B Polym. Phys.* **44**, 2935–2943 (2006).
24. Rybnikár, F. & Geil, P. Melting and recrystallization of PA-6/PA-66 blends. *J. Appl. Polym. Sci.* **49**, 1175–1188 (1993).
25. Pashaei, S., Avval, M. M. & Syed, A. A. Thermal degradation kinetics of nylon6/GF/crysnano nanoclay nanocomposites by TGA. *Chem. Ind. Chem. Eng. Q. CICEQ* **17**, 141–151 (2011).
26. Barrera, G. *et al.* Magnetic properties of nanocomposites. *Appl. Sci.* **9**, 212 (2019).
27. Karna, S. *et al.* Polymer assisted synthesis of FeNi nanoparticles. *J. Nanosci. Nanotechnol.* **10**(9), 5879–5884 (2010).
28. Barrera, G. *et al.* Verwey transition temperature distribution in magnetic nanocomposites containing polydisperse magnetite nanoparticles. *J. Mater. Sci.* **54**, 8346–8360 (2019).
29. Gupta, R., Smith, L., Njuguna, J., Deighton, A. & Pancholi, K. Insulating MgO-Al_2O_3-LDPE nanocomposites for offshore medium voltage DC cable. *ACS Appl. Electron. Mater.* **2**, 1880–1891 (2020).
30. Gupta, R. *et al.* Flexible low-density polyethylene–$BaTiO_3$ nanoparticle composites for monitoring leakage current in high-tension equipment. *ACS Appl. Nano Mater.* **4**, 2413–2422 (2021).
31. Starsich, F. H. L., Eberhardt, C., Boss, A., Hirt, A. M. & Pratsinis, S. E. Coercivity determines magnetic particle heating. *Adv. Healthc. Mater.* **7**, 1800287 (2018).
32. Parab, V. *et al.* Electric field assisted self-healing of open circuits with conductive particle-insulating fluid dispersions: Optimizing dispersion concentration. *Sci. Rep.* **9**, 19700 (2019).
33. Li, Q. *et al.* Correlation between particle size/domain structure and magnetic properties of highly crystalline Fe_3O_4 nanoparticles. *Sci. Rep.* **7**, 9894 (2017).
34. Zeleňák, V. *et al.* Large and tunable magnetocaloric effect in gadolinium-organic framework: Tuning by solvent exchange. *Sci. Rep.* **9**, 15572 (2019).
35. Mendonca, L. D., Murari, M. S. & Daivajna, M. D. Thermomagnetic correlation in La0.85-xBixNa015MnO3 soft ferromagnet due to nonmagnetic Bi3+ substitution. *J. Supercond. Nov. Magn.* **34**, 2067–2078 (2021).
36. De Oliveira, N. A. & von Ranke, P. J. Theoretical aspects of the magnetocaloric effect. *Phys. Rep.* **489**(4–5), 89–159 (2010).

Acknowledgements

The authors thank Robert Gordon University for its financial support. The authors are also grateful to the staff of the School of Engineering (David Howie, Alan Mclean, Alexander Laing, David Smith, Martin Johnstone, Alan Macpherson, and the EA Team). Additionally, the staff of the School of Pharmacy at Robert Gordon University (Laurie Smith, Bruce Petrie, Carlos Fernandez, Jenny Macaskill & Tracy Willox) for making their facility available for part of this research. Support from the Science and Technology Facilities Council (STFC) for access to facilities at the ISIS Materials Characterisation Laboratory, STFC Rutherford Appleton Laboratory (RAL) was crucial for the research presented. EPSRC is thanked for funding JAD in the JUICED Energy Hub (EP/R023662/1).

Author contributions

K.P., J.A.D. and R.G. prepared the manuscript. R.G. and G.S. carried out the magnetic characterisation. R.G. is responsible for the overall execution of the project whereas K.P. supervised the project, analysed data and conceived the overall plan and idea. J.A.D. and C.F. prepared superparamagnetic materials and contributed to manuscript preparation as well as discussion. P.G. carried out some characterisation with R.G. and proofread. Project is attached to R.G., PhD thesis, which is supervised by K.P.

Competing interests

The authors declare no competing interests.

Additional information

Supplementary Information The online version contains supplementary material available at https://doi.org/10.1038/s41598-022-14135-8.

Correspondence and requests for materials should be addressed to J.A.D. or K.P.

Reprints and permissions information is available at www.nature.com/reprints.

Publisher's note Springer Nature remains neutral with regard to jurisdictional claims in published maps and institutional affiliations.

Supplementary Data

Tuneable Magnetic Nanocomposites for Remote Self-Healing

Ranjeetkumar Gupta[1], Priya Gupta[2], Charles Footer[3], Gavin B. G. Stenning[4], Jawwad A. Darr[3]* and Ketan Pancholi[1]*

[1] School of Engineering, Robert Gordon University, Aberdeen AB10 7GE, UK
[2] Lakshmi Narain College of Technology & Sciences, RGPV, Indore, MP, India.
[3] University College London, Department of Chemistry, 20 Gordon Street, WC1H OAJ, UK.
[4] ISIS Neutron and Muon Facility, STFC Rutherford Appleton Laboratory, Didcot OX11 0QX, UK
*Correspondence: k.pancholi2@rgu.ac.uk ; Tel.: +44-1224-262317;j.a.darr@ucl.ac.uk Tel: 020 7679 4345;

SECTION 1 (S1): Materials and Methods

The steps involved in preparing the polymer magnetic nanocomposite (PMC) samples and their characterisation/testing methods are mentioned in this section.

1.1 Materials

Iron oxide MNPs (<50 nm particle size), Citric acid 99%, ε-caprolactam (CL) (99% purity), 3.0 M Ethyl Magnesium Bromide (EtMgBr) solution in diethyl ether, N-Acetyl Caprolactam (NACL) (99% purity), Ammonia solution 25% and Tetraethyl orthosilicate ≥99.0% GC (TEOS) were purchased from Sigma-Aldrich Company Ltd. Dorset, UK and used as received. Proprietary superparamagnetic nanoparticles were used as received from UCL. These are known as "SMNP" in the manuscript and were made using a process similar to that described in the experimental methods section below. The particles were characterised by having a particle size of 30 nm rhombic crystals. Deionized water with 18 MO conductivity was used throughout the experiment.

1.2 Experimental methods

i. Synthesis of SMNP nanoparticles

A schematic diagram of the reactor setup is shown in Figure S1. Two pumps (Primeroyal K, Milton Roy, Pont Saint-Pierre, France) were used to provide the supercritical water (containing 0.5 M H_2O_2) and base (1.0 M KOH) feeds at 80 and 40 mL min^{-1}, respectively (pumps P1 and P3). 10 MΩ/cm deionized water purified using a Millipore Elix® Essential water purification system was fed from pump P1 and heated to 450 °C in flow using a 7 kW custom-built electrical water heater. The metal precursor feed was pumped by P2, delivering a total flow rate 40 mL min^{-1}. The premixed precursor solutions consisted of the desired stoichiometries of each metal nitrate precursor, with a total metal salt concentration of 0.15 M. The metal precursor feed delivered from pumps P2 was first mixed with the 1.0 M KOH base feed in flow (from pump P3), before the combined mixture was introduced to a stream of supercritical water (from pump P1) in a patented Confined Jet Mixer (CJM)[1, 2]. The reaction of the precursor solutions in the CJM, resulted in the rapid crystallization of nanoparticles. The particle-containing aqueous flow was then

cooled to ca. 40 °C using a 1.5 m pipe-in-pipe heat exchange column, before passing through a back-pressure regulator (BPR). The resultant nanoparticle slurries were collected in beakers and were then cleaned by repeated centrifugation and washing with deionized water until the supernatant had conductivity below 50 µS/cm as measured using a conductivity probe (model HI98311, Hanna Instruments, Leighton Buzzard, UK). The concentrated, cleaned slurry was then freeze-dried by slowly heating from -60 °C to 25 °C, under a vacuum of <13 Pa, over 24 h using a Virtis Genesis 35XL freeze drier.

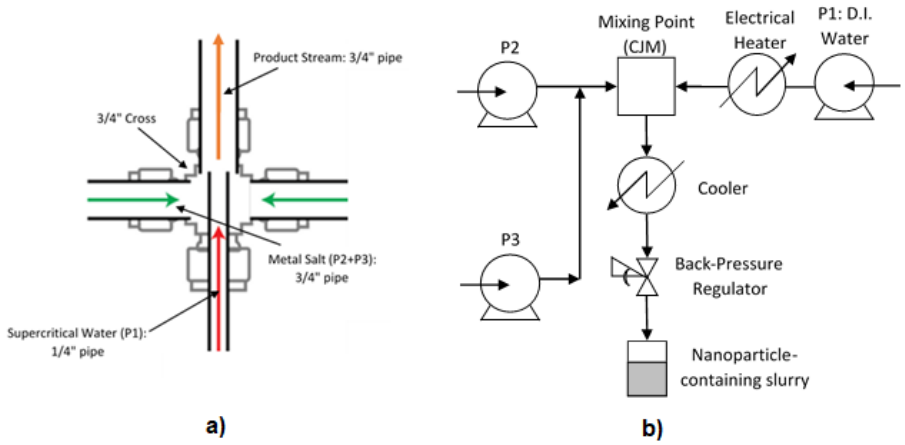

Figure S1. a) Diagram representing the confined jet mixer CJM. b) Schematic of the CHFS process, which demonstrates how the heated water from P1 is combined with the aqueous precursors from P2 and P3 at the CJM mixing point.

ii. Optimised silica functionalisation of the MNPs.

The as-received MNPs (both SMNP and Fe_3O_4) weighing 2.0 g were added to 65 mL of aqueous citric acid (0.5 g/mL concentration), associated with rigorous stirring. For effective adsorption, the pH value was adjusted to 5.2 by adding aqueous ammonia solution, which resulted in dissociation of two carboxylic groups of each of the citric acid molecules. Further adsorption was enhanced by heating to 80 °C and rigorous stirring continued for 90 min. After that, the pH was increased to 10.1, wherein the third carboxylic group of the adsorbed citric acid, was dissociated[3]. The resulting nanoparticles' have higher surface charge aiding electrostatic inter-particle repulsion and preventing agglomeration. Excess solvent was removed by centrifuging at 5000 rpm for 5 min and the collected nanoparticles were dispersed in clean DI water.

The Stöber functionalisation method was used to nucleate a silica layer on both types of MNP surfaces by first hydrolysis and then polycondensation based deposition of TEOS. It's a well-known that the hydrolysis reaction can be catalysed using acid or alkaline solvent media, whereas it is very slow in neutral conditions[4]; so aqueous NH_3 as an alkaline catalyst was used herein. The amount of TEOS to be added was calculated considering 2.4 mass ratio of MNP:TEOS. 0.85 g of TEOS dissolved in ethanol was added to the prepared suspension of magnetite MNPs; considering that the average diameter of coated MNPs are 30 nm and the used mass ratio resulted in a functionalised layer of *ca*. 2 nm (based on the surface area estimation). The pH was then stabilised at 12.0 by adding aqueous NH_3 which triggered the Stöber functionalisation reaction. The mixture was rigorously stirred for 3 hr at room temperature (RT) with probe-type 150-W sonicator (Soniprep 150; MSE., UK), giving the

MNPs a rough silica-functionalised coating. The MNPs were centrifuged at 5000 rpm for 5 min and then washed thoroughly three times with DI water. Collected MNPs were dried in oven at 120 °C under vacuum and further sieved. The finely sieved MNPs were then used in the in-situ polymerisation of the magnetic PMC synthesis. The optimised parameters of the activator and initiator used in the in-situ polymerisation were followed from a previous report[5]. The summary of the processing technique is presented in Figure S2.

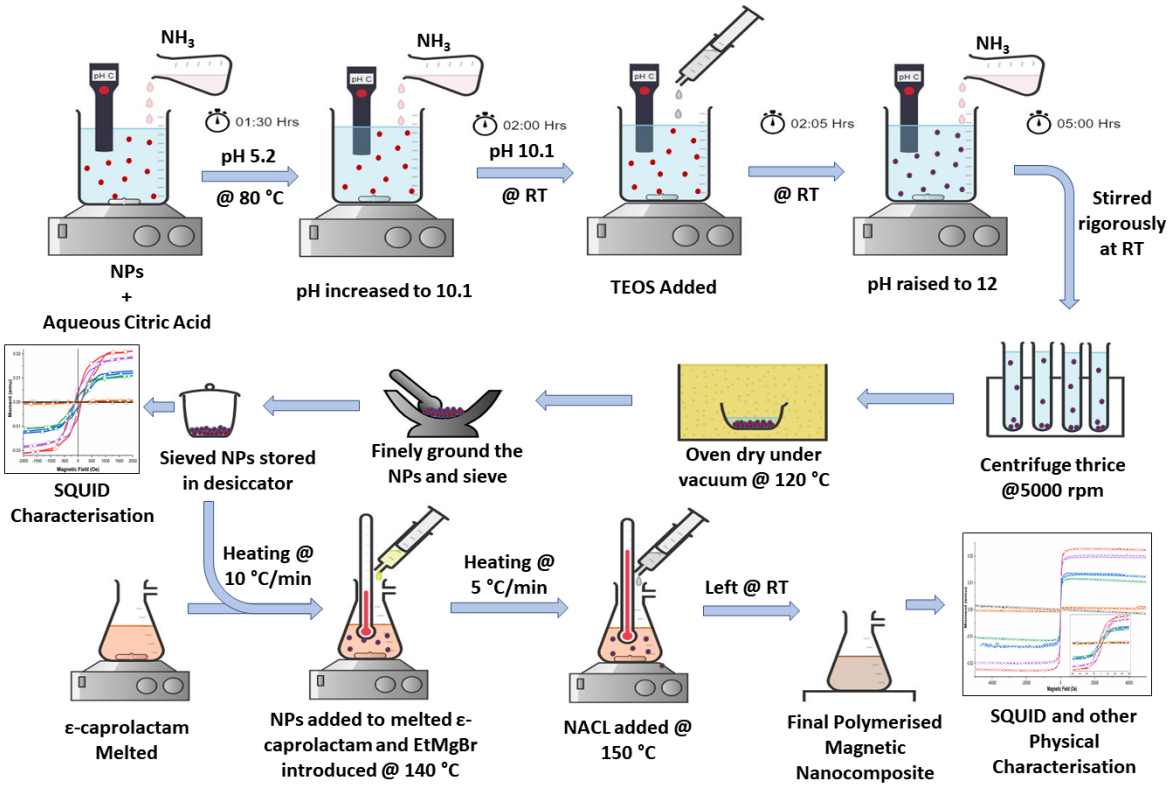

Figure S2. Experimental scheme that was followed for the functionalisation of the both types of MNPs and its subsequent usage in the in-situ polymerisation in the manufacture of magnetic nanocomposites.

iii. Characterisation methods for the functionalised MNPs and synthesised PMCs

Total four samples, as summarised in Table 1, were prepared for the characterisation study. Two samples containing 1 w/w % of silica coated SMNPs and two samples containing silica coated Fe_3O_4 were characterised using ATR-FTIR (Attenuated Total Reflection- Fourier Transmission Infrared Spectroscopy) to determine its chemical composition and confirm the successful polymerization of CL forming PA6 polymer. Previous studies have shown that the dispersion state of MNPs in the polymer, modifies the agglomerate size of the particles and degree of crystallinity of the resulting nanocomposite. To determine effect on degree of crystallinity and crystallite size, all samples were characterized using Differential Scanning Calorimetry (DSC), SAXS/WAXS and subsequent X-ray Diffraction (XRD).

1. FTIR-ATR

The nanocomposite samples were characterized using Perkin-Elmer ATR-FTIR (Attenuated Total Reflection- Fourier Transmission Infrared Spectroscope) Spectrum Gx system containing DGS-KBr sensor to identify phases and structural changes after addition of the iron oxide MNPs. In order to scan each sample, the nanocomposite films of approximately 0.1 mm thickness were prepared and total 30 scans in range of 525 to 4000 cm^{-1} were carried out at a resolution of 4 cm^{-1}. The gain was set to 2, whereas the optical velocity was fixed to 0.4747 m/s.

2. DSC

DSC was performed using a TA Instruments DSC Q100 at a heating rate of 10° C/min under a nitrogen environment with a temperature range of 20 to 270°C using a sample mass of 9 mg. The Heat/Cool/Heat standard cycle type analysis was selected for accurately depicting the behaviour and T_g and T_m for the samples prepared. The running segment consisted of a ramp heating at 10 °C/min to 250 °C, then ramp cooling at 5 °C/min to -90 °C and finally ramp heating at 10 °C/min to 250 °C. The glass transition temperature (T_g) and melting temperature (T_m) were determined from the DSC traces obtained, where the first small endothermic peak represents the glass transition temperature, and the second larger endothermic peak represents the melting temperature of the nanocomposite sample.

3. XRD

A PANalytical X'Pert Pro MPD, powered by a Philips PW3040/60 X-ray generator and fitted with an X'Celerator detector was used. Diffraction data is acquired by exposing samples to Cu-Kα X-ray radiation, which has a characteristic wavelength (λ) of 1.5418 Å. X-rays were generated from a Cu anode supplied with 40 kV and a current of 40 mA. The data were collected over a 2 theta range of 0 to 80° with a step size of 0.117° (2θ) and nominal time per step of 1099.82, using the scanning X'Celerator detector. Fixed anti-scatter and divergence slits of 0.38 mm were used together with a beam mask of 10 mm and all scans were carried out in a continuous' mode. Phase identification was carried out by means of the X'Pert-PRO accompanying software program PANalytical High Score Plus in conjunction with the JCPDS card.

4. TEM

TEM images were used to determine the morphology and mean diameter in the MNP agglomerates. TEM imaging was conducted at an accelerating voltage of 100 kV, with a spot size of 10 nm. The exposure time was varied from 0 to 50 s. The images of all samples were obtained using a Philips CM100 TEM at different direct magnifications, ranging from x7900 to x245000. An ultrathin section of nanocomposite obtained using microtome were placed on gilder grid of 400 mesh to obtain all images. For MNP imaging, the particles were dispersed in isopropyl alcohol and droplet were placed on TEM grid.

5. SAXS/WAXS

SAXS and WAXS scattering patterns were obtained on Xenocs Nano-inXider, equipped with microfocus sealed tube: Cu, 30W point focus. With Dectris Pilatus 3 hybrid photon counting (two fixed) detectors for continuous and simultaneous SAXS and WAXS acquisition up to $2\theta = 60°$. The beam path was windowless beam path, entirely under vacuum from beam delivery system to detector sensor. The SAXS patterns were obtained over a scattering vector length within the range of $0.008\ Å^{-1} < q < 0.18\ Å^{-1}$ and WAXS patterns with the range of

0.18 $Å^{-1}$ < q < 0.24 $Å^{-1}$. One-dimensional (1D) fitting of the scattering curves was obtained by an azimuthal binning and averaging of corresponding two-dimensional scattering patterns using the XSACT (X-Ray Scattering Analysis and Calculation Tool) supplied with the instruments.

6. Magnetic characterisation

Magnetisation loops of the synthesised composite samples were measured at T = 100 K and 400 K on Quantum Design MPMS XL-7, integrated with Superconducting Quantum Interference Device (SQUID) detection system and precision temperature control unit. The instrument had temperature range of 1.8 to 400 K and applied maximum field strength of ±7 Tesla with filed uniformity of 0.01% over 4 cm.

1.3 Building the 3D model interrelating with the size distribution data from physical characterisations

The TEM, XRD and SAXS results comparatively gave an estimation of the MNP/agglomerate particle size in the dispersion state. This data was input to the simulated 3D model build using a MATLAB® platform. The TEM micrographs firstly were processed in Photoshop® software; wherein they were cropped, rotated, and enlarged, for removing their edges and any distorted background. Further, they were digitally enhanced by filtering techniques for several purposes, such as removing the background noise and their artifacts or improving upon the definition and sharpness of the image. The imaged were equalized, correcting the brightness and contrast of the grayscale images, ensuring proper black and white tonalities were reached to distinguish the polymer matrix (represented by the grayscale region) and the pure black entities (representing the magnetic nanoparticles). Finally, the processed images were manually coloured, with the polymer background toned with yellow and green shade and the black nanoparticle entities toned with black and red colour representing Fe_3O_4 and CHFS made SMNP MNPs/agglomerate, respectively. Then the final toned images were saved as high quality 8-bit TIFF format and loaded in ImageJ image processing software for estimating the nanoparticles/agglomerates sizes of all the sample variations. This size data was then fed to the custom designed MATLAB® code, to be used as a basis for generating the random nanoparticles/agglomerates sizes for the simulated 3D model of the nanocomposite. The code generates the model with the required wt% of nano-inclusions and MNP/agglomerate sizes within the fed diameter range. Similar image tone allocation was followed in the processed TEM micrographs (in the simulated model as well), with black and red colour representing Fe_3O_4 and CHFS SMNP nanoparticles/agglomerates, respectively.

Section 2 (S2): Detailed analysis of SAXS data.

All obtained spectra were corrected for background scattering before any further analysis. The relation is represented by Equation S1[6] as follows:

$$I(q) = G \exp\left(-\frac{q^2 R_g^2}{3}\right) \qquad \text{Eqn. S1}$$

herein, G is the Guinier pre-factor and R_g the radius of gyration. The Guinier plot represented in Figure S3 of Section 2, of Ln I(q) vs q^2, is used to calculate the slope of the chosen region that dictates the value of R_g, giving out the MNP/agglomerate size qualitatively.

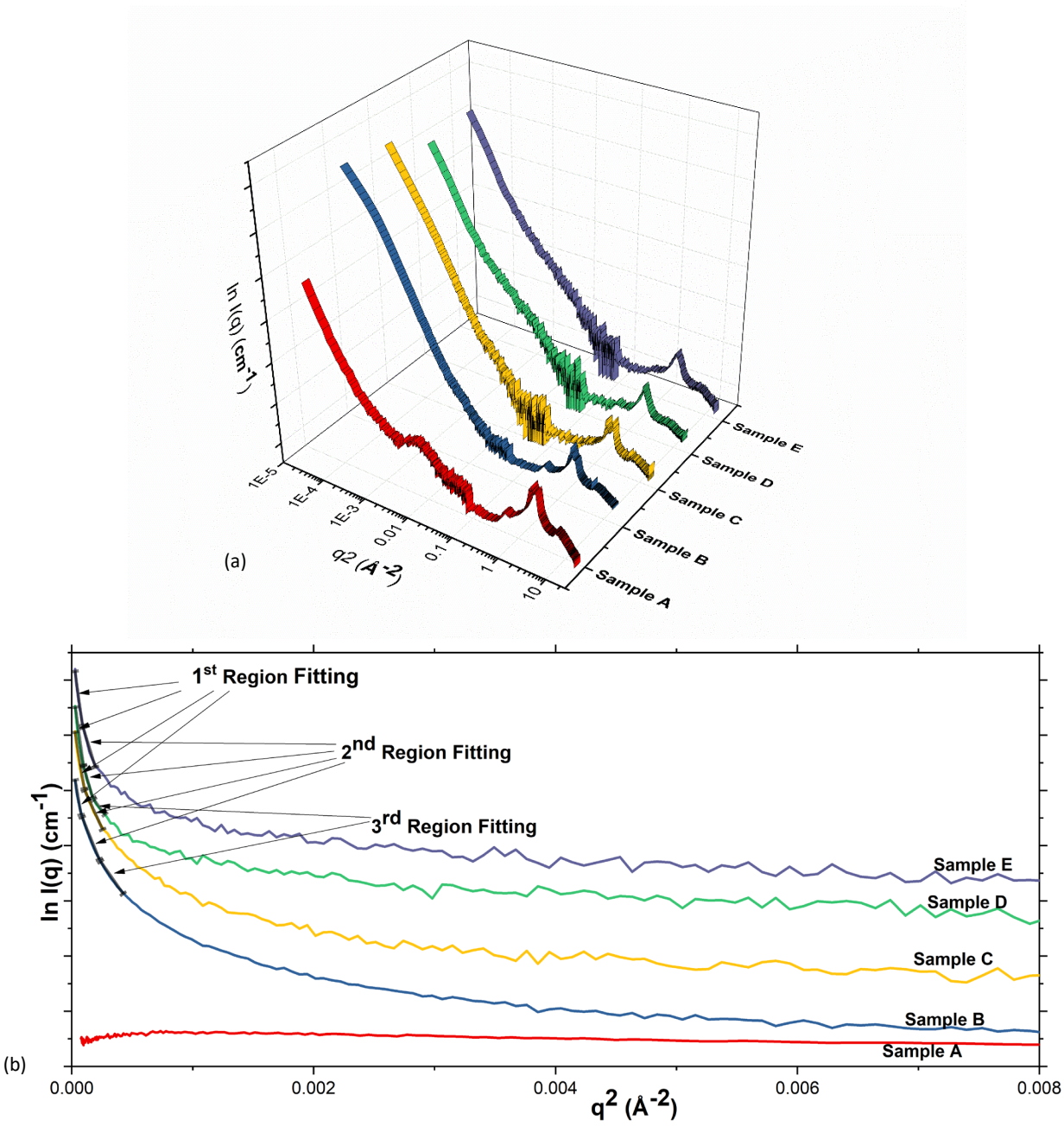

Figure S3. Guinier plot for all the samples (a), with the region fitting highlighted (b).

The MNPs are assumed as perfect sphere and the diameter D is calculated with the Equation S2[6]:

$$D = 2 \times (5/3)^{1/2} R_g \qquad \text{Eqn. S2}$$

The slope of regions in the Guinier plot were calculated to give the R_g estimate[7], this was used to calculate the diameters of the MNP/agglomerate using Equation S2. The calculated values of diameters of the MNP/agglomerate for all the SHMNP samples is summarised in Table S1 below.

Table S1: Summary of the calculated average sizes of the MNPs in each SHMNP composite sample

		sample B	sample C	sample D	sample E
1st Region Fitting	I(q) Range	0.009-0.012	0.009-0.014	0.009-0.013	0.009-0.012
	R_g	198 ± 9	150 ± 6	199 ± 10	154 ± 8
	D(nm)	58 ± 9	37 ± 6	60 ± 10	40 ± 8
2nd Region Fitting	I(q) Range	0.012-0.018	0.014-0.021	0.013-0.018	0.012-0.021
	R_g	143 ± 6	94 ± 8	145 ± 5	116 ± 5
	D(nm)	36 ± 6	25 ± 58	37 ± 5	29 ± 5
3rd Region Fitting	I(q) Range	0.018-0.022	-	0.018-0.022	-
	R_g	97 ± 4	-	90 ± 3	
	D(nm)	25 ± 4	-	24 ± 3	

Section 3 (S3): Degree of crystallinity analysis for all samples using DSC data.

The enthalpy of all the samples were calculated using the Universal Analysis software that comes along with the DSC instrument control package. By quantifying the heat associated with the melting endotherm. This heat was then reported in terms of percent crystallinity by normalizing the observed heat of fusion with that of the 100% crystalline PA6 polymer. The area used for the enthalpy (crystallinity) calculation as identified using the "Integrate Peak" functionality of the TA Universal Analysis 2000 software[8] is recreated in the plots in Figure 3 (a) (included in the main text). The same analysis also helped identify the "Melt Peak Temperature" of the endotherm peak, which was the melting point T_m of the samples and listed in the Table below. Adding to the discussion, the Glass transition temperature T_g was also identified using the "Glass/Step transition" functionality available in the same software.

The degree of crystallinity for all the samples was calculated from the following Equation 3[8], using the standard reference value of PA6 as cited in the main text.

$$Sample\ Degree\ of\ Crystallinity = \frac{Sample\ Enthalpy\ from\ DSC\ plot}{PA6\ Enthalpy\ from\ Reference\ Text} \times 100\% \qquad \text{Eqn. S3}$$

Table S2: A list of degree of crystallinity, Glass transition (T_g) and Melting temperature (T_m) from DSC results.

Sample	T_g (°C)	T_m (°C)	Enthalpy (J/g)	Degree of Crystallinity (%)
Sample A	54.7 ± 2	216.7 ± 3	99.0 ± 2	52.1 ± 2
Sample B	44.3 ± 2	212.8 ± 3	97.6 ± 4	51.4 ± 4
Sample C	46.2 ± 2	213.7 ± 2	95.3 ± 6	50.1 ± 6
Sample D	44.3 ± 1	212.6 ± 2	96.9 ± 3	51.0 ± 3
Sample E	46.5 ± 1	213.4 ± 3	93.8 ± 2	49.3 ± 2

Section 4 (S4): Crystallite size calculation for all samples using XRD data.

The crystallite sizes of MNPs were calculated from FWHM of the most intense peaks using the Scherrer formula as shown in Equation S4[9]. The Scherrer equation gives the relation between the peak width(B) and the crystallite size(L). It states that peak width is inversely proportional to crystallite size.

$$B(2\theta) = \frac{K\lambda}{L\cos\theta} \qquad \text{Eqn. S4}$$

Table S3: Crystallite sizes of MNPs calculated from FWHM of intense peaks observed in XRD.

Sample Type	Absolute Crystallite Size	
	Size(A)	Size(nm)
Sample B	456.9	45.7
Sample C	340.2	34.0
Sample D	514.7	51.5
Sample E	368.8	36.9

Ideally, PA6 contains two dominant monoclinic crystalline phases that are usually referred to as the α-phase and γ-phase. In the α-phase, which is known to be the most stable phase in terms of thermodynamics, the hydrogen bonds appear in between adjacent antiparallel chains, with the entirety of the phase attaining a trans-chain conformity[10]. This, however, is not the case in the γ-phase, as chains are seen to appear twisted in order to enable the formation of hydrogen bonds between parallel chains. Two broad peaks were seen to appear around 4.2 A° (21° 2θ) and 3.7 A° (24° 2θ) corresponds to α-crystalline phase form in PA6. The α crystalline phase dominated the crystalline structure of prepared PA6. The line at 4.2 A° referred to α1 and originated from (200) plane whereas 3.7 A° originated from (002) plane[11]. The peaks observed at 11°, 22° and 23° can be identified as the γ-phase of the of PA6 with the corresponding indexes of (020), (001) and (200)/(201)[12].

The number of unit cells (N) along their respective directions, define the broadening of the diffraction peaks. Though independent of the N, the peak area remains constant. Therefore, the peak broadening in XRD results was accompanied by decrease in the maximum peak height. However, as seen in Figure 3 (b) in main text the peaks were broadened, and intensity was decreased when silica functionalisation was employed on MNP.

There were many factors contributing to the observed peak profile. In essence, the peak profile shown in Figure 3 (b) in main text was a deconvolution of the peak from other contributions such as instrumental peak profile, crystallite size, microstrain, solid solution inhomogeneity, and temperature factors.

Section 5 (S5): Full scale plots of induced magnetisation i.e. magnetic moment as a function of applied magnetic field, showing the associated hysteresis loops in inset figures at (a) 100 K and (b) 400 K temperatures.

The SQUID characterisation results for the MNP samples are summarised as follows:

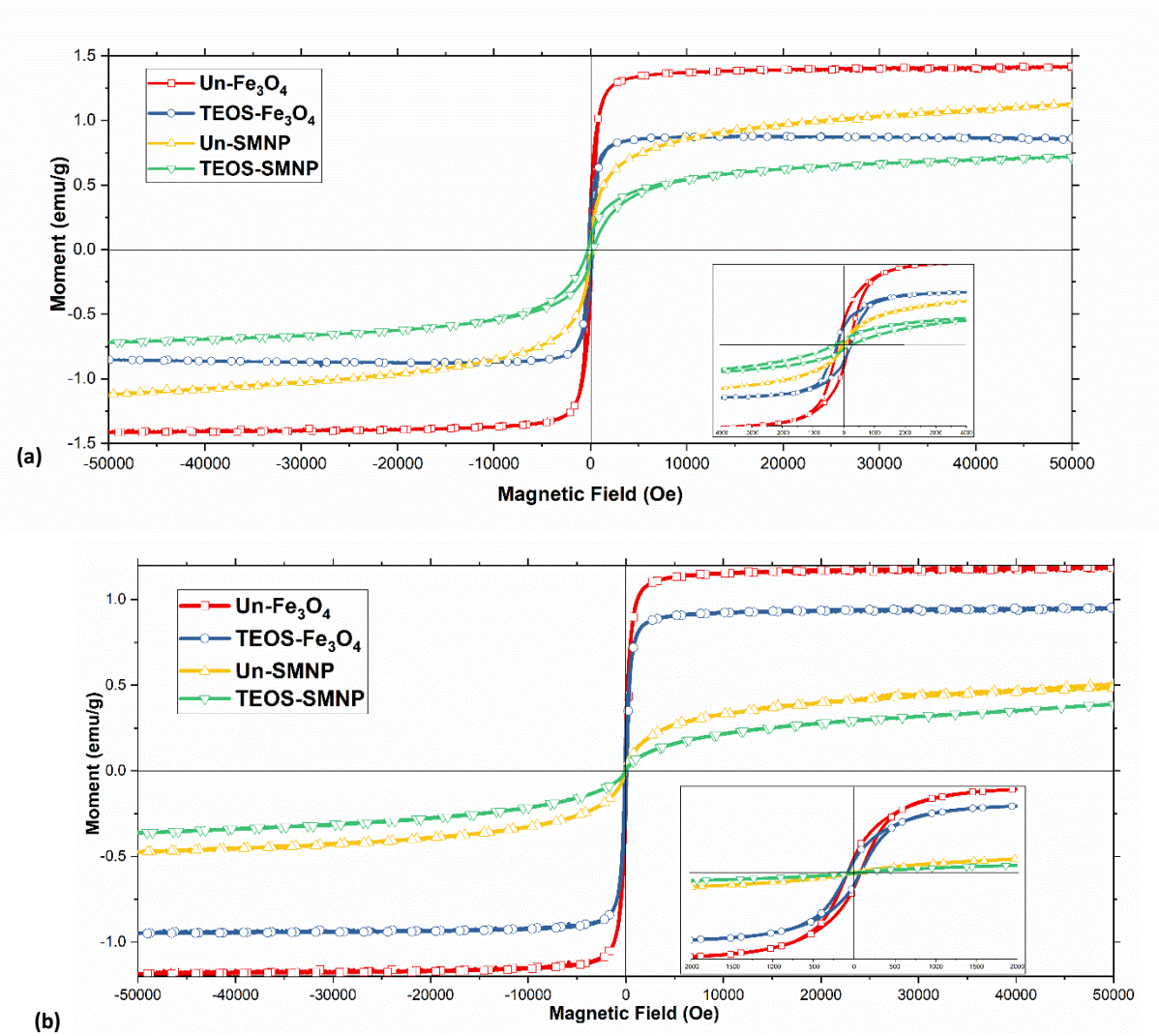

Figure S4. Full scale plots of induced magnetisation of MNPs (Magnetic moment as a function of applied magnetic field) and the associated hysteresis loops in inset figures at (a) 100 K and (b) 400 K temperatures.

Table S4: Summarised magnetic results at 100 K for uncoated MNPs and silica functionalised MNPs.

Sample	Coercivity (H_c) (Oe)	Magnetic Remanence (M_r) (emu/g)	Magnetic Saturation (M_s) (emu/g)	Magnetic Moment Ratio (M_r/M_s) (%)
Uncoated-Fe_3O_4 MNPs	238	3695 x 10^{-4}	13210 x 10^{-4}	28 ± 5
TEOS-Fe_3O_4 MNPs	224	287 x 10^{-4}	839 x 10^{-4}	34 ± 3
Uncoated-SMNP MNPs	54	493 x 10^{-4}	7275 x 10^{-4}	7 ± 6
TEOS-SMNP MNPs	261	873 x 10^{-4}	11281 x 10^{-4}	8 ± 3

Table S5: Summarised magnetic results at 400 K for uncoated MNPs and silica functionalised MNPs.

Sample	Coercivity (H_c) (Oe)	Magnetic Remanence (M_r) (emu/g)	Magnetic Saturation (M_s) (emu/g)	Magnetic Moment Ratio (M_r/M_s) (%)
Uncoated-Fe_3O_4 MNPs	82	2031 x 10^{-4}	11853 x 10^{-4}	17 ± 4
TEOS- Fe_3O_4 MNPs	81	1437 x 10^{-4}	9527 x 10^{-4}	15 ± 3
Uncoated-SMNP MNPs	29	69.17 x 10^{-4}	4806 x 10^{-4}	1 ± 5
TEOS-SMNP MNPs	22	32.95 x 10^{-4}	3623 x 10^{-4}	0.9 ± 4

The SQUID characterisation results for all the prepared nanocomposite samples are summarised as follows:

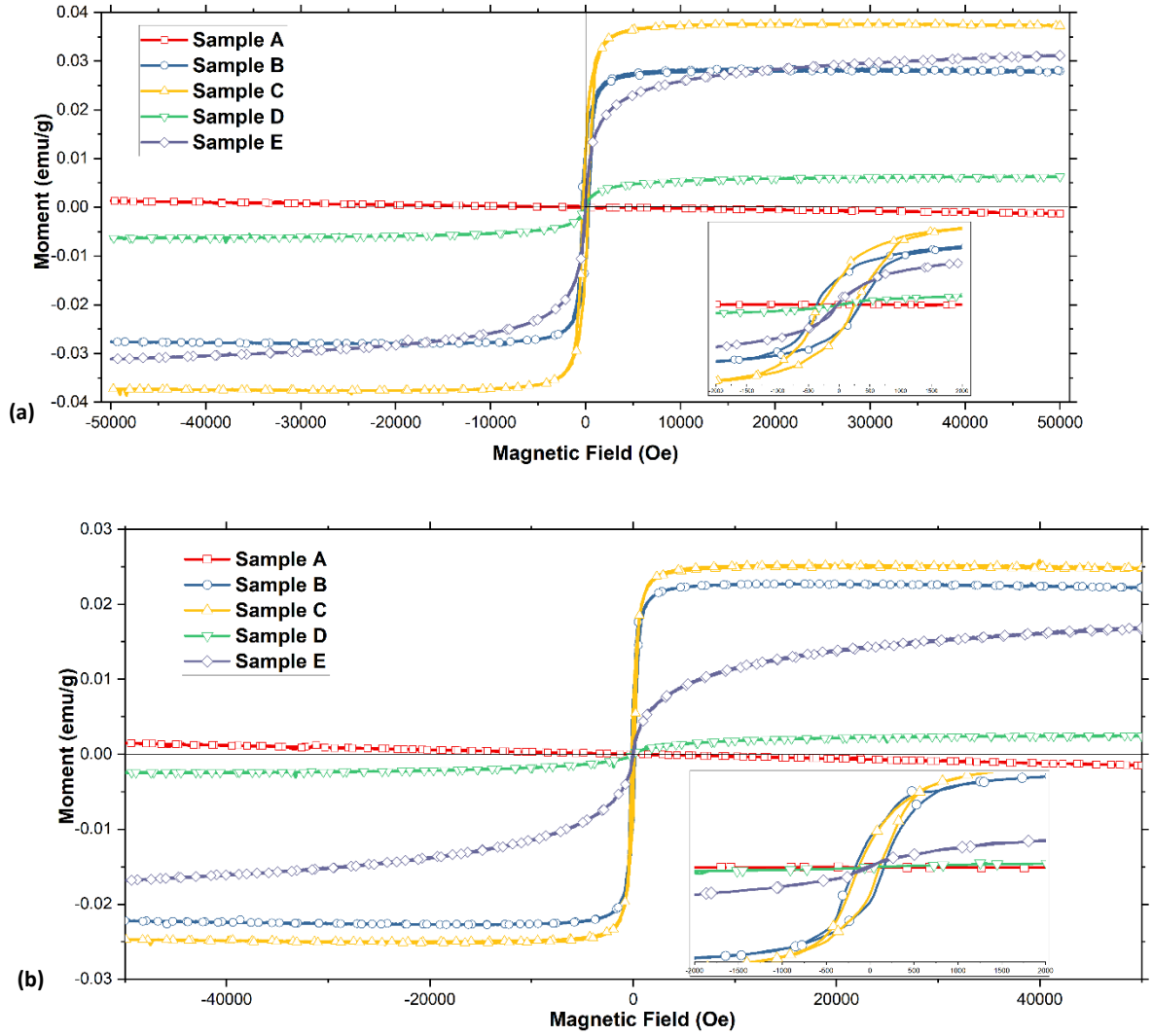

Figure S5. Full scale plots of induced magnetisation of PMC samples (Magnetic moment as a function of applied magnetic field) and the associated hysteresis loops in inset figures at (a) 100 K and (b) 400 K temperatures.

Table S6: Summarised magnetic results at 100 K for all the prepared samples.

Sample	Coercivity (H_c) (Oe)	Magnetic Remanence (M_r) (emu/g)	Magnetic Saturation (M_s) (emu/g)	Magnetic Moment Ratio (M_r/M_s) (%)
Sample A	0	0	0	0
Sample B	352	114×10^{-4}	279×10^{-4}	41 ± 4
Sample C	264	116×10^{-4}	373×10^{-4}	31 ± 3
Sample D	40	1.9×10^{-4}	63×10^{-4}	3 ± 4
Sample E	7	4.5×10^{-4}	311×10^{-4}	1 ± 5

Table S7: Summarised magnetic results at 400 K for all the prepared samples.

Sample	Coercivity (H_c) (Oe)	Magnetic Remanence (M_r) (emu/g)	Magnetic Saturation (M_s) (emu/g)	Magnetic Moment Ratio (M_r/M_s) (%)
Sample A	0	0	0	0
Sample B	162	75×10^{-4}	224×10^{-4}	33 ± 5
Sample C	117	62×10^{-4}	247×10^{-4}	25 ± 4
Sample D	39	5.3×10^{-4}	27×10^{-4}	20 ± 4
Sample E	31	4.6×10^{-4}	166×10^{-4}	3 ± 7

Section 6 (S6): Original TEM micrographs used for the Photoshop editing and Simulated Model generation.

The original TEM micrographs utilised for the analysing the agglomerates.

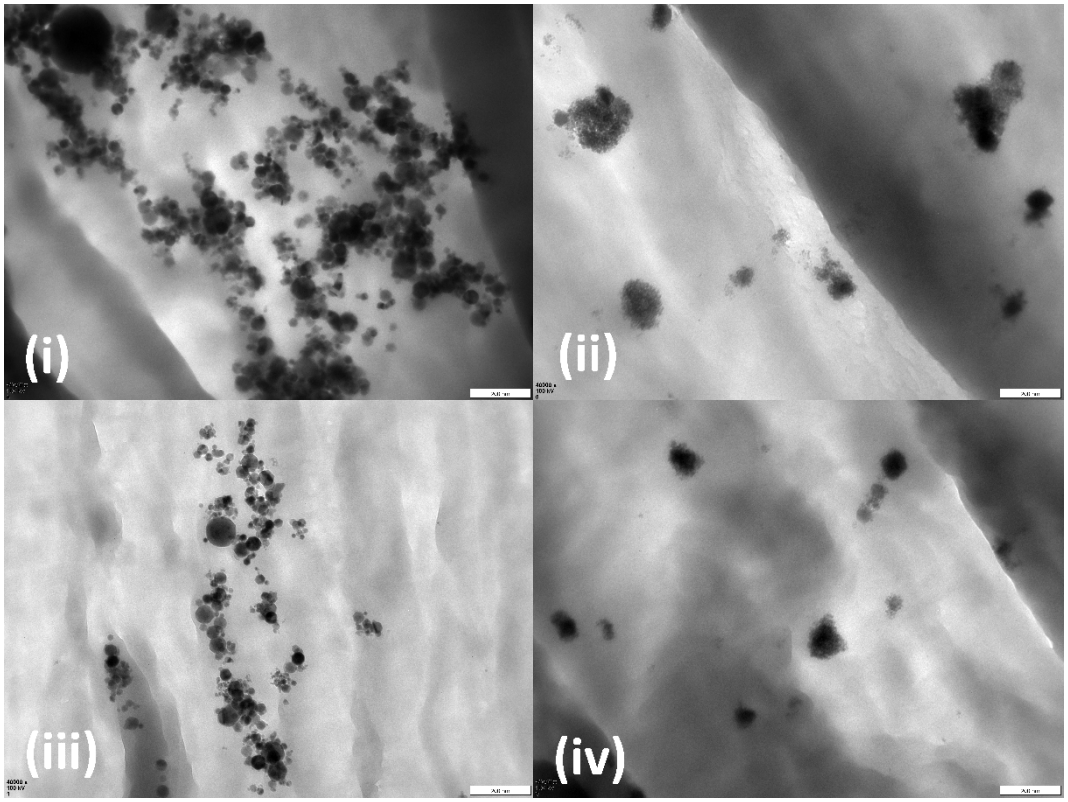

Figure S6: Original TEM micrograph images for uncoated samples (i) Sample B and (ii) Sample D; and coated samples (iii) Sample C and (iv) Sample E. (Scale bar shown is of 200 nm)

Considering all the characterisation data related with the dispersion state of the MNPs, the following summary table is prepared to be used as an input data in MATLAB® code, to simulate the 3D model.

Table S8: Estimated diameters of nanoparticle/agglomerate regions identified from TEM, SAXS and XRD.

Sample	TEM-Biggest agglomerate size (nm)	TEM-Smallest nanoparticle/ agglomerate size (nm)	SAXS calculation of nanoparticle/ agglomerate size	XRD calculation of nanoparticle/ agglomerate size
sample B	195 ± 10	25 ± 5	59	46
sample C	80 ± 15	30 ± 5	37	34
sample D	220 ± 20	50 ± 10	60	52
sample E	90 ± 10	40 ± 5	40	37

The simulated models representing the MNP/agglomerate arrangements in 3D are generated for all the samples as shown in Figure S7 below.

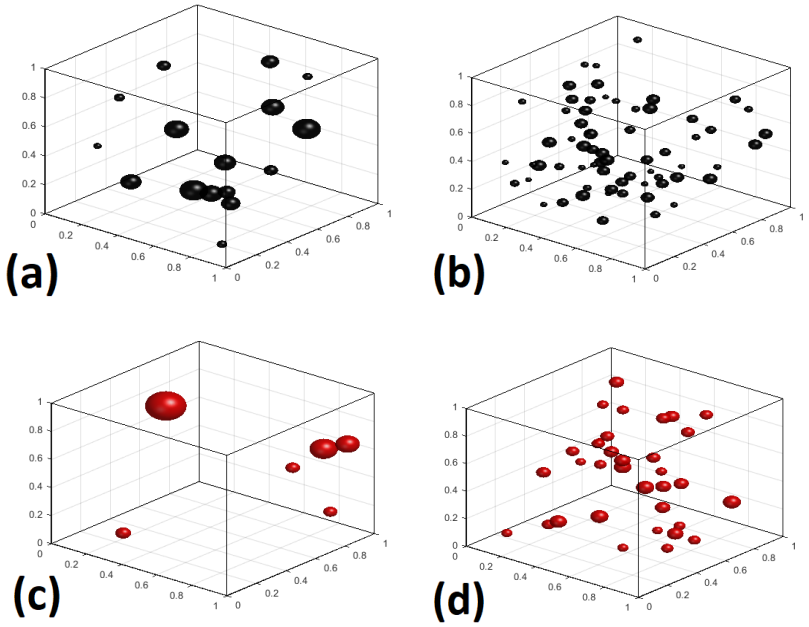

Figure S7. Simulated representation of the synthesised nanocomposite (1 cubic micron size) for Fe_3O_4 samples (a) Sample B, (b) Sample C and SMNP samples (c) Sample D, (d) Sample E respectively (Herein, Black spheres represent Fe_3O_4 and Red spheres are for SMNP nanoparticle/agglomerate respectively.)

References

1. Darr, J. A., Zhang, J., Makwana, N. M. & Weng, X. Continuous hydrothermal synthesis of inorganic nanoparticles: applications and future directions. *Chem. Rev.* **117**, 11125-11238 (2017).

2. Gruar, R. I., Tighe, C. J., Southern, P., Pankhurst, Q. A. & Darr, J. A. A direct and continuous supercritical water process for the synthesis of surface-functionalized nanoparticles. *Ind Eng Chem Res* **54**, 7436-7451 (2015).

3. Campelj, S., Makovec, D. & Drofenik, M. Preparation and properties of water-based magnetic fluids. *Journal of Physics: Condensed Matter* **20**, 204101 (2008).

4. Iler, K. R. The chemistry of silica. *Solubility, Polymerization, Colloid and Surface Properties and Biochemistry of Silica* (1979).

5. Gupta, R. *et al*. Novel Method of Healing the Fibre Reinforced Thermoplastic Composite: A Potential Model for Offshore Applications. *Composites Communications* **16**, 67-78 (2019).

6. Hino, K. *et al*. Size distribution of gold nanoparticles covered with thiol-terminated cyanobiphenyl-type liquid crystal molecules studied with small-angle X-ray scattering and TEM. *Chemical Physics Letters* **460**, 173-177 (2008).

7. Piiadov, V., Ares de Araújo, E., Oliveira Neto, M., Craievich, A. F. & Polikarpov, I. SAXSMoW 2.0: Online calculator of the molecular weight of proteins in dilute solution from experimental SAXS data measured on a relative scale. *Protein Science* **28**, 454-463 (2019).

8. Blaine, R. *Determination of polymer crystallinity by DSC.TA Instruments* (2011).

9. Speakman, S. A. Estimating crystallite size using XRD. *MIT Center for Materials Science and Engineering*, 03-08 (2014).

10. Porter, R. Macromolecular physics, volume 3—crystal melting, Bernhard Wunderlich. , 363 (1980).

11. Shete, P., Patil, R., Tiwale, B. & Pawar, S. Water dispersible oleic acid-coated Fe3O4 nanoparticles for biomedical applications. *J Magn Magn Mater* **377**, 406-410 (2015).

12. Khodabakhshi, K. Anionic polymarisation of caprolactam: an approach to optimising the polymerisation condition to be used in the jetting process. (2011).